Open Archive Toulouse Archive Ouverte (OATAO)

OATAO is an open access repository that collects the work of some Toulouse researchers and makes it freely available over the web where possible.

This is an author's version published in: https://oatao.univ-toulouse.fr/26923

Official URL: https://doi.org/10.1109/TNS.2019.2950086

To cite this version :

Le Roch, Alexandre and Virmontois, Cedric and Paillet, Philippe and Warner, Jeffrey H. and Belloir, Jean-Marc and Magnan, Pierre and Goiffon, Vincent Comparison of X-Ray and Electron Radiation Effects on Dark Current Non-Uniformity and Fluctuations in CMOS Image Sensors. (2020) IEEE Transactions on Nuclear Science, 67 (1). 268-277. ISSN 0018-9499

Any correspondence concerning this service should be sent to the repository administrator:
tech-oatao@listes-diff.inp-toulouse.fr

Comparison of X-Ray and Electron Radiation Effects on Dark Current Non-Uniformity and Fluctuations in CMOS Image Sensors

Alexandre Le Roch, *Student Member, IEEE*, Cédric Virmontois, *Member, IEEE*, Philippe Paillet, *Fellow, IEEE*, Jeffrey H. Warner, Jean-Marc Belloir, Pierre Magnan, *Member, IEEE*, and Vincent Goiffon, *Member, IEEE*

***Abstract*— This article investigates the dark current as well as the dark current random telegraph signal (RTS) after 1-MeV electron, 3-MeV electron, and 10-keV X-ray irradiations in a pinned photodiode CMOS image sensor (CIS). A large range of deposited ionizing dose from 10 to 525 krad(SiO_2) is considered. The displacement damage dose deposited through electron irradiation ranges from 60 to 1200 $TeV \cdot g^{-1}$. Results on dark current distributions highlight the predominance of the ionizing damage in opposition to the displacement damage induced by the electron irradiations. Moreover, the dark current distributions also suggest that if the ionizing dose is high enough [i.e., beyond 50 krad(SiO_2)], the trapped positive charges in the silicon oxides create high magnitude electric field regions leading to an electric field enhancement (EFE) of the dark current which is neither present at lower doses nor in pristine image sensors. This EFE mechanism also seems to have a strong influence on the RTS leading to a clear discrepancy from the existing dark current nonuniformity model developed for amplitude distributions in CISs as well as from what is reported in the literature in the more studied ionizing dose range. Annealing treatments after electron irradiations have highlighted the existence of specific population of pixels sharing the same well-defined maximum transition amplitudes (i.e., maximum amplitude between two dark current levels). The results suggest the use of maximum transition amplitude spectroscopy applied to dark current RTS to push forward the investigation on radiation-induced defects creation and identification.**

***Index Terms*— Annealing, CMOS image sensor (CIS), dark current, dark current spectroscopy (DCS), displacement damage dose (DDD), electric field enhancement (EFE), electron irradiation, pinned photodiode (PPD), random telegraph signal (RTS), total ionizing dose (TID), X-ray irradiation.**

A. Le Roch, P. Magnan, and V. Goiffon are with the Institut Supérieur de l'Aéronautique et de l'Espace (ISAE-SUPAERO), Université de Toulouse, F-31055 Toulouse, France (e-mail: alexandre.le-roch@isae-supaero.fr).

C. Virmontois and J.-M. Belloir are with the Centre National d'Etudes Spatiales (CNES), F-31400 Toulouse, France.

P. Paillet is with Commissariat à l'Energie Atomique et aux énergies alternatives (CEA), Direction des Applications Militaires (DAM), DIF, F-91297 Arpajon, France.

J. H. Warner is with the U.S. Naval Research Laboratory, Washington, DC 20375 USA.

Digital Object Identifier 10.1109/TNS.2019.2950086

I. Introduction

HIGH total ionizing dose (TID) effects are becoming prominent for radiation test standards as well as for the qualification of electronic systems required for emerging applications. These days, high TID tolerance represents one of the biggest challenges for CMOS image sensors (CISs), being devices with growing interest for future space missions and nuclear experiments. On the one hand, driven by space research activities, upcoming space exploration programs such as Jupiter's moons missions are requiring high TID tolerance (i.e., few Mrad) [1]. On the other hand, strategic interests requiring TID tolerance up to 100 Mrad are also growing concerning the improvement of nuclear power plant reliability [2], the development of fusion reactors such as International Thermonuclear Experimental Reactor (ITER) [3], and scientific experiments dedicated to the study of matter based on particle detection at the High Luminosity Large Hadron Collider (HL-LHC) [4]. All these emerging projects demonstrate the need to enhance the ionizing dose tolerance for CIS. The comparison between X-ray and electron effects on CIS dark current is motivated by the necessity to be more representative of the space environments involving electron exposures such as Jupiter's moons exploration [1]. The motivation to investigate electron irradiations also lies in the need to understand the displacement damage mechanisms induced by electron irradiations and to highlight their different recoil defects compared to those induced by neutron and proton irradiations, being the usual testing species for displacement studies. Due to the lower non-ionizing energy loss (NIEL) of electrons compared to protons and neutrons for a given energy, the structure of the defects created for a given displacement damage dose (DDD) can be very different. Because of the light mass of electrons and their negative charge, electron irradiations mostly lead to elastic Coulombic interactions with silicon nuclei. On the other hand, protons above 10 MeV and neutron irradiations lead to elastic nuclear collisions with strong nuclear interactions and even inelastic nuclear reactions for neutrons and protons above 20 MeV. Hence, electron irradiations are more likely induce either isolated defects, also called point defects, or small clusters which are small aggregates of defects due to the limited energy transferred to

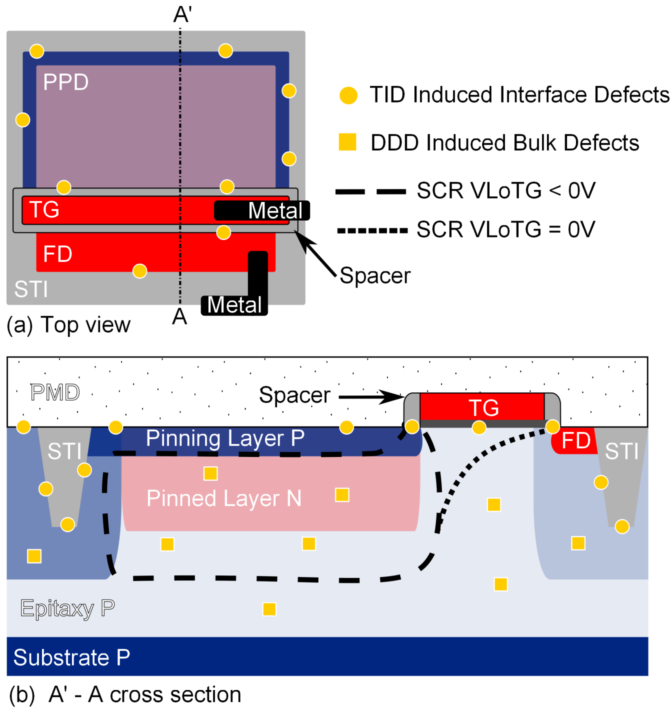

Fig. 1. (a) Top-view and (b) cross section of at PPD pixel illustrating the interface defects as well as the bulk defects locations after deposition of an ionizing and a displacement dose. The PPD SCR for two TG bias conditions is illustrated in dashed lines.

the primary knock-on atom (PKA) of silicon. Particles with higher NIEL like neutrons or protons rather create clusters of defects which become more and more complex as the particle energy increases. The remaining question in this field of investigation is how the radiation-induced defect structure impacts the degradation of the device's characteristics, such as the dark current in CIS. This degradation factor is also referred to as the damage factor [5].

Fig. 1 depicts both TID-induced interface defects and DDD-induced bulk defects in a cross section of a pinned photodiode (PPD) CIS. In the case of pure TID exposure as X-ray irradiations, only interface defects are created. When located in depleted regions, those defects act as generation centers leading to a dark current increase. In the case of electron beam exposure whose energy is sufficient to displace silicon atoms (i.e., a few MeV), both ionizing deposition and displacement damage are involved. Hence, both interface defects and bulk defects are created and participate in the dark current increase when located in the depleted regions. The dark current can also present some discrete and random fluctuations called the random telegraph signal (RTS), leading to blinking pixels and preventing the calibration of the CIS. This article focuses on the radiation-induced dark current distribution over the sensor array as well as the distribution of the RTS maximum transition amplitude (i.e., maximum amplitude between two dark current levels) beyond 100 krad(SiO_2); a TID range which has not been well explored yet.

II. Experimental Details

To extend the understanding of TID effects on CIS to the high TID range, three X-ray irradiations have been performed on a four-transistor (4-T) PPD CIS with TID ranging from 10 to 500 krad(SiO_2). Also, to provide new insights into the dark current increase induced by electron irradiations, one 1-MeV electron and four 3-MeV electron irradiations have been performed with TID ranging from 26 to 525 krad(SiO_2) and DDD ranging from 60 to 1200 TeV $\cdot$ g^{-1}. Finally, to compare with usual radiation tests, the last irradiation using 22-MeV neutrons has been performed. This article is completing the results reported in [6] on a 3T CIS by exploring the effects on a 4-T PPD CIS which is the considered technology for Europa's mission.

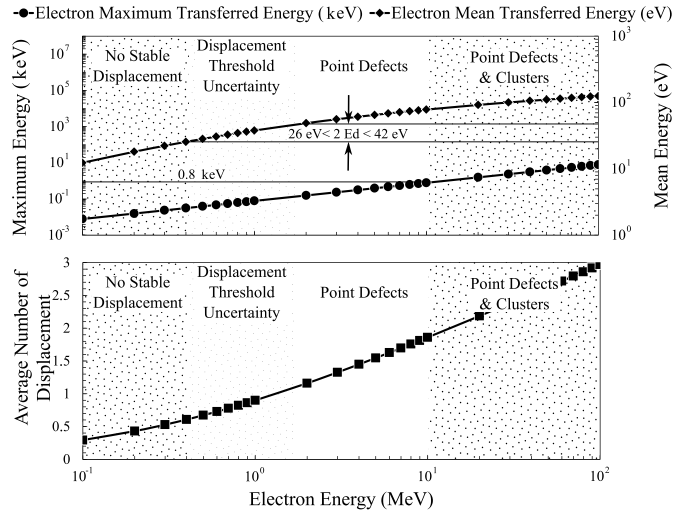

Fig. 2. Average number of stable displaced silicon atoms [8] as a function of the electron energy computed from the mean and the maximum transferred energy.

The electron irradiations aim to achieve high TID as well as to focus on point defect creation. Hence, low-energy electron irradiations are considered. However, a minimum energy labeled E_d is required to displace a silicon atom from its crystal site. The most commonly used threshold energy is $E_d = 21$ eV, but values between $E_d = 13$ eV and $E_d = 25$ eV may be found in [7]. This leads to a compromise between sufficiently low energy to avoid cluster formation and sufficiently high energy to create displacement. As introduced in [8], the average number of stable displaced silicon atoms can be estimated using the mean energy transferred T_{mean} from an impinging electron to a silicon atom through Coulomb elastic scattering

$$T_{mean} = \frac{E_d T_{max}}{T_{max} - E_d} \ln\left(\frac{T_{max}}{E_d}\right) \tag{1}$$

where the maximum transferred energy to a nucleus of mass M (i.e., 28.085 u for silicon) by an electron of mass $m_e = 5.49 \times 10^{-4}$ u of energy E is defined as

$$T_{max} = \frac{2(E + 2m_e c^2)}{Mc^2} E. \tag{2}$$

Fig. 2 presents the average number of stable displaced silicon atoms as a function of the electron energy computed from the mean and the maximum transferred energy. According to [8], 1- and 3-MeV electrons should produce a majority

TABLE I

IRRADIATION PARAMETERS

Sensor Ref	A	B	C	D	E	F	G	H	I
Particle	Electron	Electron	X-ray	X-ray	X-ray	Electron	Electron	Electron	Neutron
Energy (MeV)	3	3	10×10^{-3}	10×10^{-3}	10×10^{-3}	3	3	1	22
Fluence (cm^{-2})	1×10^{12}	2×10^{12}	-	-	-	4×10^{12}	2×10^{13}	4.5×10^{12}	1×10^{11}
DDD ($TeV.g^{-1}$)	60	120	-	-	-	240	1200	126	519
TID (krad(SiO_2))	26.2	52.5	10	100	500	105	525	113	-

of point defects. Uncertainty on the previously mentioned minimum energy labeled E_d leads to an electron energy range where stable displacement may or may not happen. The 1-MeV electron irradiation test has been chosen to verify the minimum energy threshold in this energy range.

The CIS under test is a 4-T PPD custom imager manufactured in a commercially available 180-nm CIS technology. The CIS array comprises 512×512 pixels with a pitch of 7 μm and a PPD-depleted volume of 23 μm^3. This sensor has been designed and built for scientific research purposes allowing the control of the transfer gate (TG) potential during the integration. The structure of the pixels is similar to the illustration presented in Fig. 1.

The X-ray irradiations were performed using an Aracor mono-energetic 10-keV X-ray irradiator at commissariat à l'energie atomique et aux énergies alternatives (CEA) direction des applications militaires (DAM) in Bruyère le Chatel, France. The electron irradiations were performed at Mercury Plastics electron radiation facility located in Middlefield, OH, USA. The flux ranged from 4×10^{10} to 1×10^{13} $cm^{-2} \cdot s^{-1}$ depending on the electron target fluence. The fluence levels ranged from 1×10^{12} to 2×10^{13} cm^{-2} ($\pm 10\%$), which corresponds to a TID ranging from 26.2 to 525 krad(SiO_2). The sample temperature increased from 28 °C to 35 °C for the highest flux and fluency-level exposure. The neutron irradiation has been performed at Université Catholique de Louvain (UCL) in Louvain, Belgium. The neutron beam is a spectrum centered on 22 MeV but spreads from 10 to 40 MeV with a flux of 1.67×10^8 $cm^{-2} \cdot s^{-1}$. Irradiation parameters are summarized in Table I, and all of the exposures were performed on a different CIS at room temperature with all CIS pins grounded.

All of the measurements have been performed in the dark at 22 °C in a temperature-controlled chamber after four weeks of room temperature annealing. The dark current measurements use ten integration times from a few milliseconds to two seconds. Each image attributed to a given integration time is built from the average image of ten acquisitions to reduce the temporal noise. The dark current is computed as the slope of the output voltage as a function of the integration time using a charge to voltage factor (CVF) of 13.5 $\mu V/e^-$. The dark current RTS analysis method uses a rising edge detection algorithm over 15 000 images with a 1-s sampling time as introduced in [9] and further developed in [10]. During the integration, while thermally generated charges are collected in the PPD, the TG bias is kept at its low level to isolate the PPD from the floating diffusion (FD). This TG low-level bias labeled V_{LoTG} impacts the electric-field distribution into the photodiode. In this article, the influence of the electric field on the PPD dark current is investigated using the TG low-level bias from 0.2 to −1 V. Varying the TG potential allows evaluating the contribution of the interface defects located under the gate oxide.

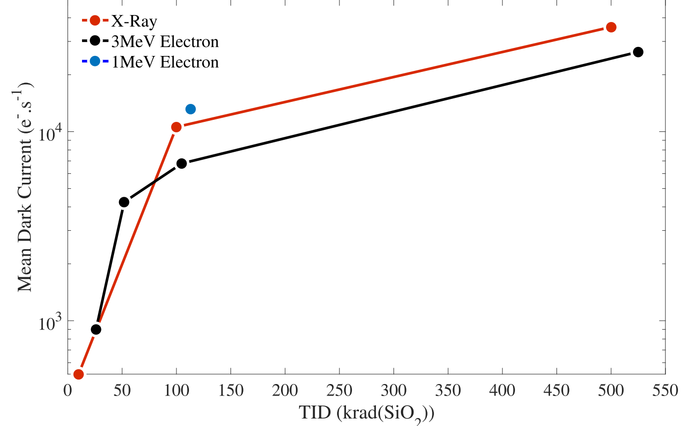

Fig. 3. Evolution of the mean dark current at $V_{LoTG} = 0$ V over the CIS array with the deposited TID for electron and X-ray irradiations.

III. Radiation-Induced Mean Dark Current

The evolution of the mean dark current over the CIS array with the deposited TID at $V_{LoTG} = 0$ V is reported in Fig. 3. For TID until 100 krad(SiO_2), the dark current after electron and X-ray irradiations is comparable and reaches a few thousand of electrons per second. In this TID range, results on mean dark current are comparable to those found in PPD CIS in [11] and [12]. When increasing the deposited dose to 500 krad(SiO_2), X-ray irradiation reveals a higher dark current than the one after electron irradiation at 525 krad(SiO_2). This result could be linked to a sensor design variability and this observation requires more tests with TID between 100 and 500 krad(SiO_2) as well as a statistical approach to confirm this difference. However, one of the explanations could be the difference in terms of electron/hole pair recombination rate either related to the dose rate difference between the irradiation facilities or to the density of pairs created by the incident radiation. Similar observations have been highlighted for Co^{60} gamma rays and 10-keV X-rays in [13]. The pair density is determined by the linear energy transfer (LET) and is, therefore, a function of the incident particle type and energy [14]. The dark current difference observed in Fig. 3 between the 525-krad(SiO_2) electron and the 500-krad(SiO_2) X-ray irradiations suggests a higher electron/hole pair density for the electron irradiation leading to a greater recombination process and, therefore, to a lower degradation. This trend is also observed for the 100-krad(SiO_2) X-ray and the 105 krad(SiO_2) 3-MeV electron irradiations. Moreover, it could also explain the higher degradation

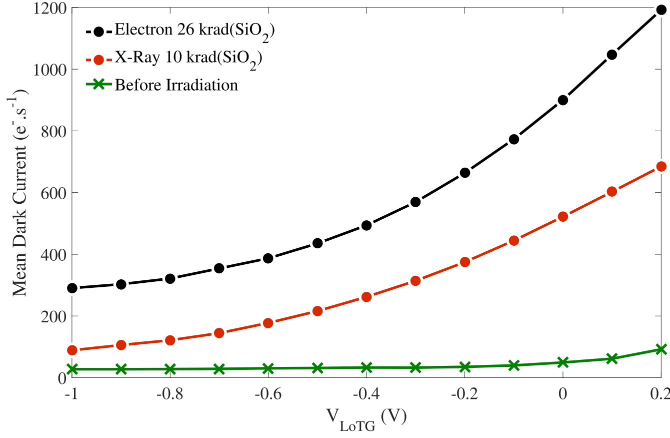

Fig. 4. Evolution of the mean dark current over the CIS array with the applied TG bias during the integration before and after low TID electron and X-ray irradiations.

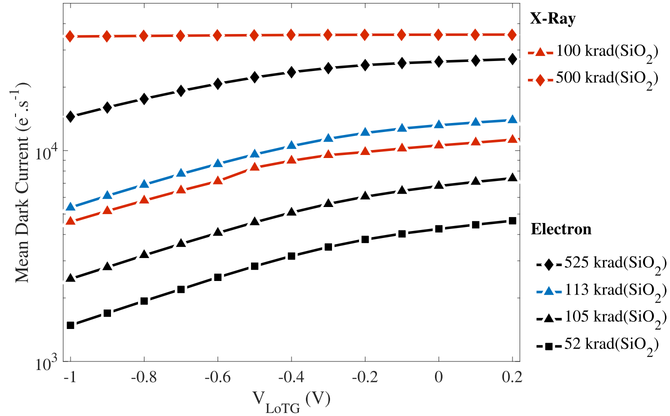

Fig. 5. Evolution of the mean dark current over the CIS array with the applied TG bias during the integration after high TID electron and X-ray irradiations.

observed for the 1-MeV electron irradiation compared to the 3-MeV electron irradiation knowing that 1-MeV electrons have a lower LET than 3-MeV electrons (i.e., $\text{LET}_{1\text{ MeV}} = 1.57 \times 10^3\ \text{KeV} \cdot \text{cm}^2.\text{g}^{-1}$ and $\text{LET}_{3\text{ MeV}} = 1.64 \times 10^3\ \text{KeV} \cdot \text{cm}^2 \cdot \text{g}^{-1}$).

The evolution of the mean dark current with the applied TG bias during the integration before and after electron and X-ray irradiations is visible in Figs. 4 and 5. The dark current induced by the irradiations is visible, and thus for all the applied TG bias. As shown in Fig. 4, lowering the TG bias from +0.2 to −1 V reduces the mean dark current by 70% before irradiation. After 10-krad(SiO_2) X-ray and 26-krad(SiO_2) electron irradiations, the dark current reduction caused by the negative TG voltage reaches 85% and exhibits the same shape as in [11], [12], and [15]. In Fig. 5, the weakening of the TG influence on the dark current with the deposited TID is also observed but with less effectiveness. The TG-induced reduction of the dark current reaches 60% after 100 krad(SiO_2), and only 10% after 500-krad(SiO_2) deposition. The accumulation regime under the gate oxide can explain the dark current reduction with negative TG bias. For negative TG bias, the space charge region (SCR) does not merge with the interface states under the gate oxide, preventing the PPD from collecting generated carriers. This bias condition is illustrated

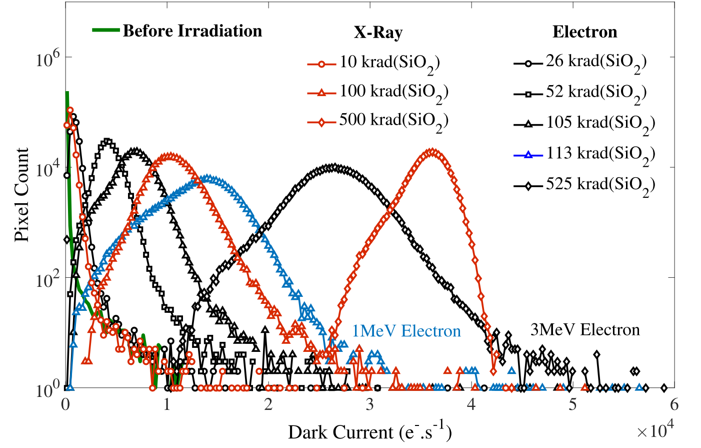

Fig. 6. Dark current distributions before and after X-ray and electron irradiations at $V_{\text{LoTG}} = 0$ V.

in Fig. 1(b). When the TG is grounded (i.e., 0 V TG bias), the SCR extends under the TG and allows the PPD to collect the charges coming from the interface generation centers. This bias condition is illustrated in Fig. 1(b). As the deposited TID increases, the modulation rate of the dark current with the TG bias condition is less effective until reaching a few percent. These results suggest that the deposited TID creates other dark current sources which are not impacted by the TG bias condition. For high TID, the induced dark current sources most probably come from the oxide spacers surrounding the TG, which are not impacted by the TG bias and where interface states are already known as high defect density regions after ionizing exposure [15] as illustrated in Fig. 1.

IV. Radiation-Induced Dark Current Distributions

The dark current distributions before and after X-ray and electron irradiations are presented in Fig. 6. The dark current distributions reveal Gaussian-like distributions for both X-ray and electron irradiations. These Gaussian distributions have been observed and attributed to the TID contribution in several articles [6], [16], [17]. It is clear that the mean dark current increases with the deposited TID but differences remain visible between X-ray and electron irradiations as seen in Fig. 3 at $V_{\text{LoTG}} = 0$ V and commented in Section III.

The DDD is known to lead to a large dark current nonuniformity in PPD CIS [18]. The absence of hot pixel tails after electron irradiations in Fig. 6 suggests that the TID is the dominant dark current contribution for all irradiations. It is not surprising for X-ray irradiations, which cannot lead to any atomic displacement. However, 1- and 3-MeV electron irradiations are known to deposit a significant displacement contribution as discussed in Section II and reported in [19] and [20]. Hence, despite the admitted high sensitivity of PPD CIS to displacement damage, the DDD-induced by the considered 1- and 3-MeV electron irradiations are not visible in the dark current distributions.

The TID and the DDD dark current distribution models that have proved to be representative of the results usually reported in the literature [21] are used to discuss the shape of

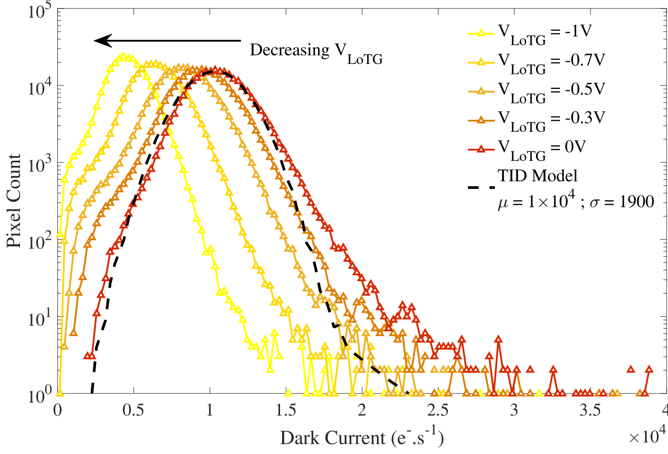

Fig. 7. Evolution of the dark current distribution after X-ray irradiation at 100 krad(SiO_2) with the applied TG bias. The Gaussian-based TID model is plotted in the black dashed line for grounded TG.

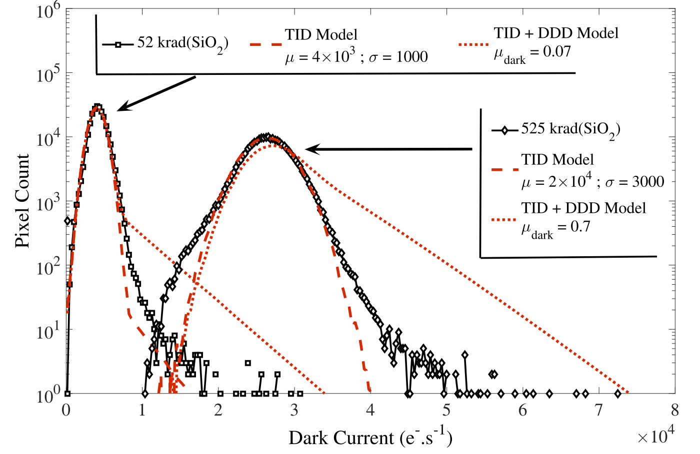

Fig. 8. Dark current distribution after electron irradiation at 52 and 525 krad(SiO_2) at $V_{LoTG} = 0$ V. The Gaussian-based TID models with and without the DDD contribution are plotted in red dashed lines.

the distributions. Considering one pixel after X-ray irradiation, the dark current $I_{dark_{TID}}$ can be expressed as

$$I_{dark_{TID}} = I_{dark} + \Delta I_{dark_{TID}} \tag{3}$$

with I_{dark} being the dark current before irradiation and $\Delta I_{dark_{TID}}$ being the TID-induced dark current increase occurring from the sum of the contributions of each generation center created by the TID. Using the probability density function (pdf) to study the whole population of the pixels over the sensor array, (3) becomes

$$f_{dark_{TID}}(x) = f_{dark}(x) + f_{\Delta I_{dark_{TID}}}(x) \tag{4}$$

with $f_{dark_{TID}}(x)$ being the so-called TID model, $f_{dark}(x)$ as the pre-irradiation pdf, and $f_{\Delta I_{dark_{TID}}}(x)$ as the Gaussian-based distribution whose input parameters are the experimental mean and standard deviation of the dark current.

Fig. 7 shows the experimental data and the Gaussian-based TID model for grounded TG after X-ray irradiation at 100 krad(SiO_2). By comparing the model to the experimental data, a fairly good agreement is observed for the majority of the pixels. However, a slight discrepancy is highlighted for a small population of the pixels presenting high dark currents. This mismatch could be interpreted as an electric-field enhancement (EFE) of a small population of pixels where defects are impacted by TID-induced high electric-field regions, as discussed in [22]–[24].

The evolution of the dark current distribution with the applied TG bias is also reported in Fig. 7. As already pointed out in Fig. 5, the entire distribution is shifted toward lower dark currents lowering the average dark current value. Results on electron irradiations are similar and are not reported here for the sake of clarity. The TG bias does not have any impact on the hypothetical EFE discussed earlier. In addition to a global reduction of the dark current, decreasing TG bias suggests the existence of a new population of pixels presenting low dark current at the left of the distribution. The origin of this pixel population, which is more influenced by the TG electric field than the other pixels, is under investigation.

Fig. 8 shows the experimental data and the model accounting for both TID and DDD for the case of a grounded TG after electron irradiations at 52 and 525 krad(SiO_2), respectively. To account for both TID and DDD contributions in the dark current distribution, a mixed model is introduced in (5) and labeled $f_{dark_{TID+DDD}}(x)$. This model is built from the previously mentioned TID model in (4) labeled $f_{dark_{TID}}(x)$ and the DDD contribution labeled $f_{dark_{DDD}}(x)$

$$f_{dark_{TID+DDD}}(x) = f_{dark_{TID}}(x) * f_{dark_{DDD}}(x). \tag{5}$$

The DDD-induced leakage current distribution labeled $f_{dark_{DDD}}(x)$ in (5), as introduced in [21], is based on an exponential PDF law. By comparing the prediction model to the experimental data in Fig. 8, it is visible that the dark current prediction model tail related to the DDD is overestimating the experimental data. These results suggest that the prediction model developed from proton and neutron irradiations does not account for displacement degradations induced by the considered electron irradiations. The lower displacement damage factor attributed to the electrons in comparison to the protons and neutrons as reviewed in [5] could explain this result. Therefore, it confirms that the DDD model developed for 1- to 100-MeV protons and neutrons is not applicable for 1- and 3-MeV electrons. This observation is not surprising since the same effect is well known in the universal damage factor (UDF) [25]. Finally, only the TID-induced dark current contribution is observed after electron irradiation and discloses a strong similarity with the pure-TID degradations induced by X-ray irradiations.

To prove the existence of displacement damage after electron irradiations in our devices, two 30-min annealing treatments have been performed at 200 °C and 280 °C. Results on 100-krad(SiO_2) X-ray, 105 krad(SiO_2) 3-MeV electron, and 113 krad(SiO_2) 1-MeV electron irradiations are presented and compared to the pre-irradiation result in Fig. 9. On the other hand, the X-ray irradiation only reveals a single dark current peak corresponding to the remaining TID contribution, and the electron irradiations hint at a larger dark current tail attributed to the displacement damage. As reported in [26] and [27], the recovery of the TID-induced defects starts at a lower temperature than the DDD bulk defects allowing

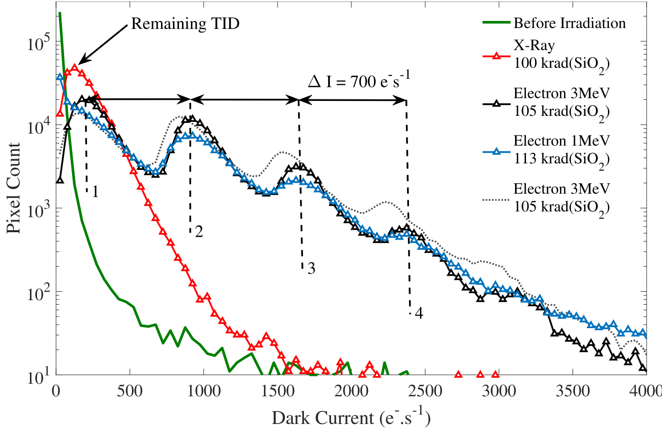

Fig. 9. Dark current distributions at $V_{\mathrm{LoTG}} = 0$ V after X-ray and electron irradiations and an annealing treatment at 200 °C and 280 °C.

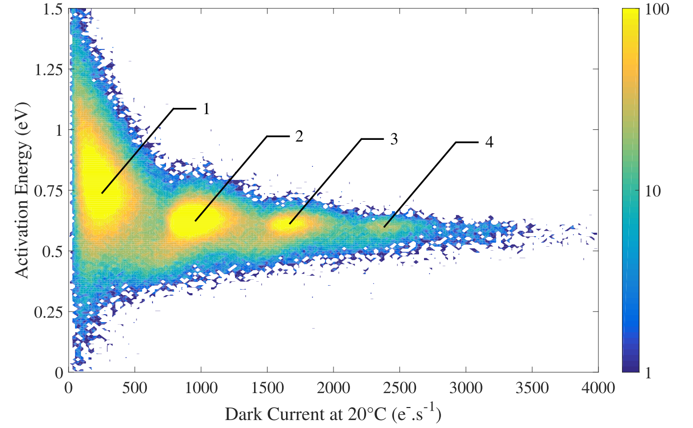

Fig. 10. Dark current activation energy at $V_{\mathrm{LoTG}} = 0$ V after 105 krad(SiO_2) 3 MeV electron irradiation and the 30-min annealing treatment at 200 °C plotted at 22 °C.

faster annealing of the TID contribution and to reveal the displacement damage contribution. Moreover, the dark current distributions after the 3- and 1-MeV electron irradiations disclose the same four dark current spikes labeled 1, 2, 3, and 4. Despite the mixed contribution between the DDD and the renaming TID, the peaks referred to as 2, 3, and 4 have a large DDD contribution corresponding to bulk defect generation signatures. The smaller amount of defects observed for 1-MeV electron irradiation lies in the smaller deposited DDD (i.e., 126 $\mathrm{TeV} \cdot \mathrm{g}^{-1}$) compared to the one deposited by the 3-MeV electron irradiation (i.e., 240 $\mathrm{TeV} \cdot \mathrm{g}^{-1}$). These generation peaks are observed at different dark current values which take multiple values of a constant dark current increase of $\Delta I = 700\ \mathrm{e}^{-} \cdot \mathrm{s}^{-1}$. After the 30-min annealing treatment at 280 °C, those generation spikes are still present for the two electron irradiations, as shown in Fig. 9 in dashed lines for the 3-MeV electron irradiation. This typical generation dark current signature has already been observed in PPD CIS after alpha particle irradiations [27] and after low energy and end-of-range (EOR) proton irradiations [28], [29] at the same dark current values and the same annealing treatments. It is not surprising to see similar results for low energy proton, alpha particle, and electron irradiations as they both involve the same displacement mechanisms known as elastic Coulombic interactions leading to a majority of point defects. These defects are not identified yet. Moreover, their formation could be strongly dependent on the annealing treatment, which enhances the mobility of the point defects enabling them to form complex stable structures [30], [31].

Finally, the considered electron irradiations deposited a significant DDD as expected. It confirms that before annealing, the TID is the predominant dark current source compared to the displacement damage contribution. Combined with a lower damage factor attributed to electron irradiations, the overall dark current distribution is similar to a Gaussian-like distribution. Concerning the minimum energy E_{d}, it is clear that 1-MeV electrons with a mean transferred energy of $T_{\mathrm{mean}} = 38$ eV are able to form stable displacements. It emphasizes that the minimum energy to displace a silicon atom is about $E_{\mathrm{d}} = 19$ eV. It is important to keep in mind that this result is based on an estimation method developed in [8] and does not provide sufficient precision to account for the exact minimum energy as it is related to complex mechanisms [7].

The dark current activation energy after the 105 krad(SiO_2) 3-MeV electron irradiation and the 30-min annealing treatment at 200 °C has been computed using the Arrhenius expression at 22 °C and 32 °C. The per-pixel activation energy is then plotted as a function of its per-pixel dark current value at 22 °C in Fig. 10 where the color scale follows the frequency. As commonly observed in CIS and dark current spectroscopy (DCS), high dark current pixels have activation energies close to 0.6 eV and are called mid-gap defects. The previously observed dark current spikes in Fig. 9 (i.e., 1, 2, 3, and 4) are also visible in Fig. 10 with the color scale. The dark current generation peaks referred to as 2, 3, and 4 with the highest DDD contribution share the same activation energy at 0.63 eV confirming the presence of the same defects highlighted in [27]–[29] at the same activation energy. With a temperature of formation close to 200 °C and a similar activation energy, oxygen-based point defects (i.e., V_2O, V_2O_2) could be one of the responsible structures for these dark current signatures [30], [31].

V. Radiation-Induced Dark Current RTS

As commonly observed after irradiation in CIS, some pixels reveal random and discrete fluctuations of their dark current called RTS. Each RTS pixel has a maximum transition amplitude corresponding to the highest dark current evolution between two dark current levels. Fig. 11 shows the distributions of the maximum transition amplitude over the CIS array after electron and X-ray irradiations. RTS pixels are already visible after the lowest doses. Similar RTS amplitude distributions are observed for the 26-krad(SiO_2) electron and the 10-krad(SiO_2) X-ray irradiations. As the deposited TID increases, the total number of RTS pixels increases as well as the mean maximum transition amplitude. For higher doses, for both electron and X-ray irradiations, the RTS amplitude distributions reveal an unusual increasing tail far from the typical slope of $A_{\mathrm{RTS}} = 110\ \mathrm{e}^{-} \cdot \mathrm{s}^{-1}$ observed in CIS [10], [32].

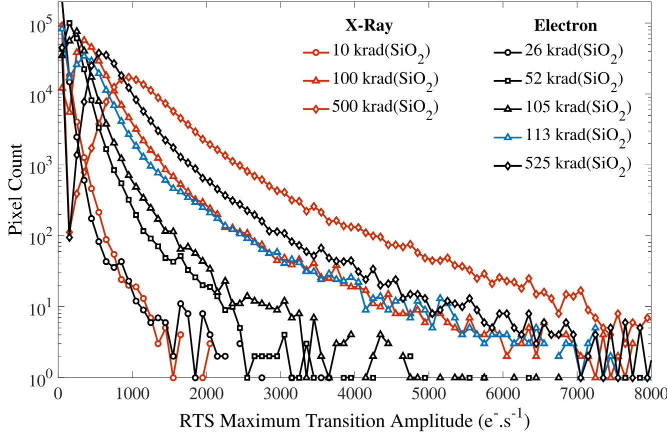

Fig. 11. RTS maximum transition amplitudes distribution after electron and X-ray irradiations.

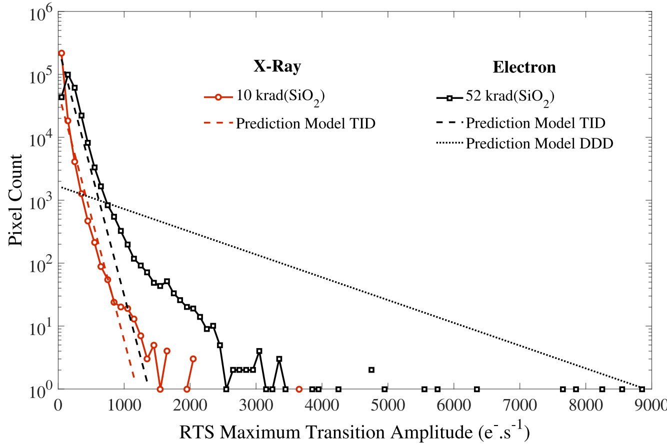

Fig. 12. RTS maximum transition amplitudes distribution and prediction models for low TID irradiations.

Moreover, the typical DDD contribution at $A_{\mathrm{RTS}} = 1200\ \mathrm{e}^{-}{\cdot}\mathrm{s}^{-1}$ after the electron irradiations is not visible. This result completes the results of Section III, where the DDD contribution induced by the electron irradiations was not visible on the dark current distributions.

To further discuss the RTS amplitude distributions, the experimental data are compared to the RTS amplitude prediction model. Fig. 12 shows the RTS maximum transition amplitude distributions after X-ray and electron irradiations at 10 and 52 krad(SiO_2), respectively. Regarding the 10-krad(SiO_2) X-ray distribution, which is similar to the 26-krad(SiO_2) electron irradiation as shown in Fig. 11, the TID prediction model is in good agreement with the data. For higher TID after electron irradiation at 52 krad(SiO_2), the prediction model still fits the majority of the pixels but starts to underestimate the end of the distributions. This discrepancy from the prediction can be attributed to an EFE enhancing RTS amplitudes. Finally, the prediction model is confirmed for TID until 50 krad(SiO_2). Nevertheless, the prediction model accounting for DDD-RTS amplitude distribution highly overestimates the data after electron irradiation at 52 krad(SiO_2). As discussed for the dark current distributions, the DDD

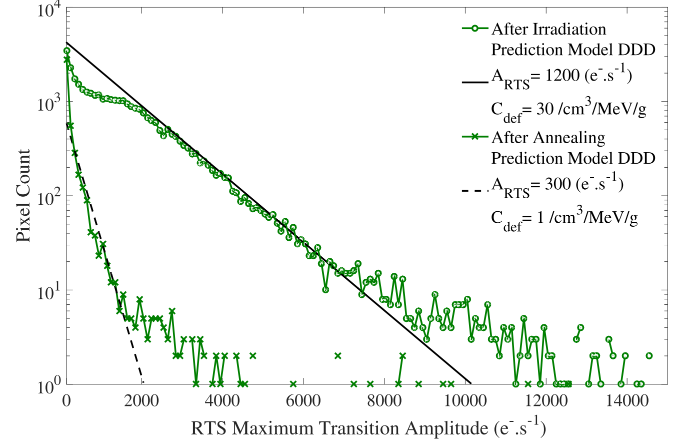

Fig. 13. RTS maximum transition amplitude distributions for 519 $\mathrm{TeV} \cdot \mathrm{g}^{-1}$ neutron irradiation before and after a 30-min annealing treatment at 200 °C.

induced by the considered electron irradiation is not visible on RTS amplitude distribution either.

Finally, the RTS distributions seem to be more impacted by an EFE when the TID increases, as shown in Fig. 11. Results suggest that, as observed in Section IV for dark current, the RTS-TID is the dominant contribution for electron irradiations. Moreover, a TID-induced electric field seems to bend the RTS distribution making the DDD contribution challenging to observe. In addition to a lower damage factor attributed to electron irradiations, all of these effects prevent the visualization of the DDD contribution, leading to very similar results between X-ray and electron irradiations.

As discussed in Section IV, RTS distributions are studied after 30-min annealing at 200 °C. To be more representative of what is reported in the literature, the RTS maximum transition amplitude distribution after neutron irradiation is shown in Fig. 13. Fig. 13 presents the results after 30-min annealing at 200 °C. Before annealing, the RTS prediction model is in good agreement with the experimental data and reveals the characteristic mean RTS amplitude at $1200\ \mathrm{e}^{-} \cdot \mathrm{s}^{-1}$ as already shown in numerous articles [33]. After annealing, the RTS pixel frequency is reduced, suggesting a reduction in the number of RTS defects per unit volume and per DDD labeled C_{def} [34]. A reduction in the mean RTS amplitude is also observed and reaches $300\ \mathrm{e}^{-} \cdot \mathrm{s}^{-1}$. This mean amplitude reduction either lies in the faster recovery of the clusters with the highest RTS amplitudes, or a global reduction of the clusters RTS amplitudes.

Results on 100-krad(SiO_2) X-ray and 105-krad(SiO_2) electron irradiations are shown in Fig. 14. In contrast to the X-ray irradiation showing the remaining RTS-TID contribution, the electron irradiation reveals a higher RTS amplitude tail related to the deposited DDD. Furthermore, the displacement contribution after electron irradiation also hints at two RTS spikes labeled B and C in Fig. 14. These DDD-RTS spikes are related to a specific population of RTS pixels with a well-defined RTS maximum transition amplitude. In the same figure, the prediction model applied to the electron irradiation is based on the neutron irradiation results shown in Fig. 13 at similar DDD and after the same 30-min annealing treatment

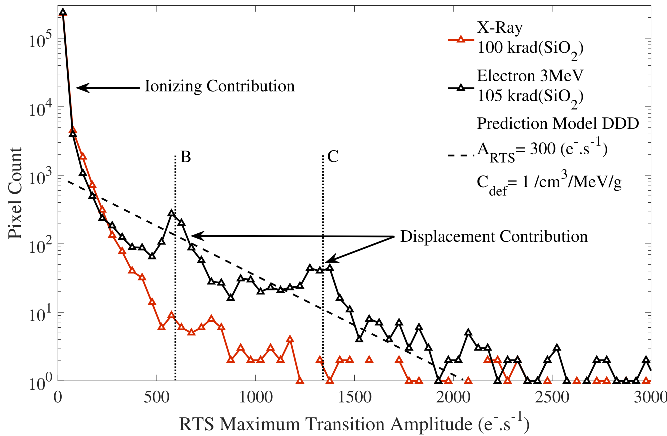

Fig. 14. RTS maximum transition amplitude distributions for 100 krad(SiO_2) X-ray and 105 krad(SiO_2) electron irradiations after a 30-min annealing treatment at 200 °C. The prediction model is based on the neutron irradiation results shown in Fig. 13 at similar DDD and after the same 30-min annealing treatment at 200 °C.

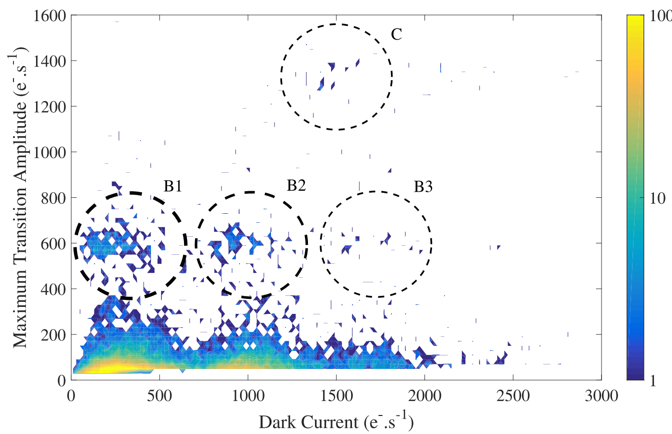

Fig. 15. RTS maximum transition amplitude as a function of the dark current all over the sensor array after electron irradiation at 105 krad(SiO_2) and a 30-min annealing treatment at 200 °C.

at 200 °C. A fairly good agreement with the experimental data is observed, suggesting the existence of two RTS populations (i.e., C and B) within a continuous RTS amplitude distribution similar to neutron irradiation results.

The RTS maximum transition amplitude is plotted as a function of the dark current for each pixel all over the sensor array in Fig. 15. The color scale follows the pixel frequency. As previously observed in the dark current distribution in Fig. 9, the dark current spikes (i.e., 1, 2, and 3) are visible. On the other hand, the RTS maximum transition amplitude spikes highlighted in Fig. 14 (i.e., B and C) are also visible. Finally, Fig. 15 allows observation of the correlation between the RTS maximum transition amplitude and the dark current leading to the identification of four populations labeled B1, B2, B3, and C. What is interesting is that the pixel population including defects responsible for the dark current peaks 1, 2, and 3 seems to comprise a fraction of RTS pixels with all of the same maximum transition amplitude. These results emphasize the existence of defects with a constant and characteristic dark current and a small fraction of them with an RTS behavior disclosing a characteristic maximum transition amplitude.

This new maximum transition amplitude spectroscopy applied to dark current RTS allows the cross-correlation between the dark current and the RTS behavior. It can be a powerful tool in the investigation of defects in semiconductors.

VI. Discussion

A. TID-Induced EFE

There is a fundamental difference between the dark current and the RTS analysis in the method used to measure the dark current value and the RTS maximum transition amplitude. On the other hand, the RTS maximum amplitude is measured by extracting from each RTS trace the most significant transition, the dark current value is the sum of all dark current sources in the same pixel. Therefore, the dark current value comes from a multitude of dark current sources, whereas the RTS maximum transition amplitude only accounts for the more active RTS center per pixel. When the TID increases, the evolution of the RTS maximum transition amplitude distribution results in an upward shift of the RTS histogram, as shown in [32]. However, as observed in Fig. 11, the TID increase leads to an overall bending of the distribution. Following this observation, it suggests a redistribution of the involved electric fields into the PPD structure leading to high-magnitude electric-field regions. Coupling with the high concentration of interface defects created at high TID, an EFE could impact the RTS amplitudes. This EFE induced by the oxide spacer trapped charges is hardly visible on the dark current distributions because the contribution of the numerous low-intensity generation centers hides the very few generation centers boosted by the EFE existing in the same depletion volume. It leads to an averaging of the overall dark current value of each pixel. The TCAD simulation results on electric-field distribution into the PPD structure are presented in Fig. 16. Before irradiation, a small region with a high electric field is visible in Fig. 16(b) and results from the overlap between the gate and the pinned layer. After TID deposition, a positive trapped charge in oxides leads to a high-magnitude electric-field region which is particularly visible under the oxide spacer in Fig. 16(c). Results confirm the existence of an EFE in the studied 4T PPD structure after high TID deposition.

B. Electron Damage Factor

The predominance of the TID contribution on the overall dark current could be reduced with radiation-hardened photodiodes [2]. Another method to study displacement damage after low-energy electron irradiation could be the use of more energetic electrons whose NIEL is higher and more effective to displace silicon atoms [8]. However, cluster formation needs to be avoided as well as high TID deposition, which tends to increase with energy following the LET. The difficulty in observing the displacement damage contribution in the dark current distribution also lies in the NIEL scaling concept. When a constant damage factor is observed to be invariant with the particle type and energy, the NIEL scaling concept is said to apply [5]. The underlying principle is that the same degradation will occur in devices exposed to the same DDD. It results in a linear dependence of the damage factor with the

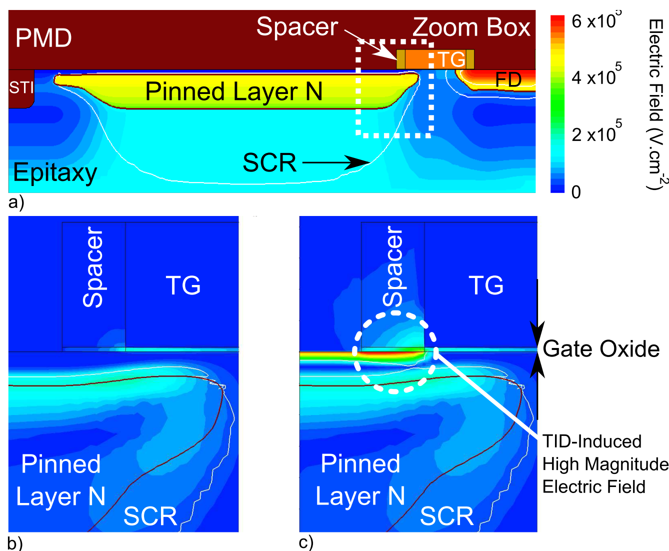

Fig. 16. TCAD simulation based on the 4-T PPD structure illustrated in (a) implants, (b) distribution of the electric field around the PPD during integration before irradiation, (c) distribution of the electric field around the PPD during integration after irradiation. The latter simulation has been performed with a trapped charge density of $N_{\mathrm{ot}} = 4 \times 10^{12}$ cm^{-2} [35]. The TG is biased in accumulation (i.e., negative gate voltage).

NIEL as reported for proton and neutron irradiations. However, it has been reported that the NIEL scaling approach does not apply to electrons with energies lower than 10 MeV for which the damage factor follows a quadratic dependence on the NIEL.

C. Point Defects and Clusters

The minimum energy threshold E_{d} as well as the NIEL of considered electron energies are also important concepts to discuss. Indeed, a few studies have reported different NIEL values for low energy electrons with the so-called effective NIEL approach based on molecular dynamics simulations [36]. Results emphasize lower NIEL (i.e., effective NIEL) compared to those usually found in the literature. It could result in a lower deposited DDD in the tested devices. Moreover, in the same approach, the minimum energy threshold E_{d} is profoundly impacted and can reach only a few electron volts. These results emphasize more significant displaced Si atoms for the considered electron energy and suggest the existence of small clusters rather than a majority of point defects as expected. However, these assumptions still need to be verified experimentally.

D. Annealing Effects and Maximum Transition Amplitude Spectroscopy

The annealing treatments performed in this article have revealed the displacement contribution induced by the electron irradiations. However, neither the dark current nor the RTS amplitude distributions allow concluding on the structure of the defects. Similarities in the RTS amplitude distributions between neutron and electron irradiations after annealing emphasize common recovering mechanisms probably related to clusters recovering. On the other hand, the RTS amplitude spikes only observed for the electron irradiation strongly supports the existence of specific RTS populations either related to point defects or small clusters. Annealing treatments play a crucial role in defect identification and become even more appealing to develop further when focusing on the RTS maximum transition amplitude spectroscopy. The recovery dynamics also need to be considered. Indeed, the complexity of the thermal-assisted defect creation and reaction at high temperatures remains an essential issue for radiation-induced defect identification. Future studies need to consider long-term annealing with lower temperatures. Finally, after DDD deposition in CIS, the origin of the tail visible in dark current distributions and RTS maximum transition amplitude distributions are always the result of a multiplicity of very different structures of defects creating a continuous distribution. Annealing treatments tend to rearrange the structures of defects in more stable configurations allowing hints of a specific population of defects. These specific structures of defects certainly participate in the overall distribution after irradiation, but are not the only defects responsible for the global RTS behavior since other RTS centers can participate, resulting in a multitude of maximum transition amplitudes.

VII. Conclusion

This article confirms that the effectiveness of negatively biased TG to reduce dark current is reduced when the TID increases. Furthermore, it reveals that TID-induced dark current distributions in PPD CIS remain mainly Gaussian at high TID. Even though PPD CISs are more sensitive to displacement damage compared to conventional photodiode based image sensors, results on dark current distributions highlight the predominance of the ionizing damage toward the displacement damage induced by the electron irradiations. Despite the resulting modification of the PPD electrostatic potential structure, the TID-induced dark current distribution does not seem impacted. On the contrary, TID-induced RTS maximum transition amplitude distributions are strongly affected by this high-magnitude electric-field region caused by the oxide spacer trapped charges. As direct consequences, these results highlight that for application involving TID above 50 krad like the Jupiter's moons missions (i.e., a few Mrad), TID-induced RTS can be a significant issue due to trapped charges in oxide spacers inducing an EFE.

The annealing treatments have highlighted the displacement damage contribution in the dark current distributions as well as in the RTS maximum transition amplitude distributions after the electron irradiations. A comparison with the X-ray irradiation at similar TID and the neutron irradiation at similar DDD has confirmed the existence of RTS populations with a specific maximum transition amplitude. Results suggest the use of maximum transition amplitude spectroscopy applied to dc-RTS to push forward the investigation on radiation-induced defect creation and identification.

Acknowledgment

The authors would like to thank O. Marcelot from ISAE-SUPAERO for having made the TCAD simulation possible.

REFERENCES

[1] C. Paranicas, J. F. Cooper, H. B. Garrett, R. E. Johnson, and S. J. Sturner, "Europa's radiation environment and its effects on the surface," Europa, Univ. Arizona Press, Tucson, Arizona, Tech. Rep., 2009, pp. 529–544. [Online]. Available: https://www.researchgate.net/profile/H_Garrett/publication/252679357_Europa's_Radiation_Environment_and_Its_Effects_on_the_Surface/links/5484e09a0cf24356db60e328.pdf

[2] V. Goiffon *et al.*, "CAMRAD: Development of a multi-megagray radiation hard CMOS camera for dismantling operations," in *Proc. Dismantling Challenges, Ind. Reality, Prospects Feedback Exper. (DEM)*, Avignon, France, vol. 50, no. 17, Oct. 2018. [Online]. Available: https://oatao.univ-toulouse.fr/23023/

[3] J. Verbeeck *et al.*, "Qualification method for a 1 MGy-tolerant front-end chip designed in 65 nm CMOS for the read-out of remotely operated sensors and actuators during maintenance in ITER," *Fusion Eng. Des.*, vols. 96–97, no. 28, pp. 1002–1005, Oct. 2015.

[4] F. Faccio, S. Michelis, D. Cornale, A. Paccagnella, and S. Gerardin, "Radiation-induced short channel (RISCE) and narrow channel (RINCE) effects in 65 and 130 nm MOSFETs," *IEEE Trans. Nucl. Sci.*, vol. 62, no. 6, pp. 2933–2940, Dec. 2015.

[5] J. R. Srour and J. W. Palko, "Displacement damage effects in irradiated semiconductor devices," *IEEE Trans. Nucl. Sci.*, vol. 60, no. 3, pp. 1740–1766, Jun. 2013.

[6] M. Beaumel, D. Hervé, and D. V. Aken, "Cobalt-60, proton and electron irradiation of a radiation-hardened active pixel sensor," *IEEE Trans. Nucl. Sci.*, vol. 57, no. 4, pp. 2056–2065, Aug. 2010.

[7] J. Bourgoin and M. Lannoo, *Point Defects in Semiconductors II: Experimental Aspects*. New York, NY, USA: Springer-Verlag, 1983. [Online]. Available: https://link.springer.com/book/10.1007%2F978-3-642-81832-5

[8] G. H. Kinchin and R. S. Pease, "The displacement of atoms in solids by radiation," *Rep. Prog. Phys.*, vol. 18, no. 1, pp. 1–51, 1955.

[9] V. Goiffon, G. R. Hopkinson, P. Magnan, F. Bernard, G. Rolland, and O. Saint-Pe, "Multilevel RTS in proton irradiated CMOS image sensors manufactured in a deep submicron technology," *IEEE Trans. Nucl. Sci.*, vol. 56, no. 4, pp. 2132–2141, Aug. 2009.

[10] C. Durnez, V. Goiffon, C. Virmontois, J.-M. Belloir, P. Magnan, and L. Rubaldo, "In-depth analysis on radiation induced multi-level dark current random telegraph signal in silicon solid state image sensors," *IEEE Trans. Nucl. Sci.*, vol. 64, no. 1, pp. 19–26, Jan. 2017.

[11] V. Goiffon *et al.*, "Identification of radiation induced dark current sources in pinned photodiode CMOS image sensors," *IEEE Trans. Nucl. Sci.*, vol. 59, no. 4, pp. 918–926, Aug. 2012.

[12] V. Goiffon *et al.*, "Radiation effects in pinned photodiode CMOS image sensors: Pixel performance degradation due to total ionizing dose," *IEEE Trans. Nucl. Sci.*, vol. 59, no. 6, pp. 2878–2887, Dec. 2012.

[13] J. M. Benedetto and H. E. Boesch, "The relationship between 60Co and 10-keV X-ray damage in MOS devices," *IEEE Trans. Nucl. Sci.*, vol. NS-33, no. 6, pp. 1317–1323, Dec. 1986.

[14] T. R. Oldham and F. B. McLean, "Total ionizing dose effects in MOS oxides and devices," *IEEE Trans. Nucl. Sci.*, vol. 50, no. 3, pp. 483–499, Jun. 2003.

[15] C. Durnez *et al.*, "Total ionizing dose radiation-induced dark current random telegraph signal in pinned photodiode CMOS image sensors," *IEEE Trans. Nucl. Sci.*, vol. 65, no. 1, pp. 92–100, Jan. 2018.

[16] C. Virmontois *et al.*, "Dose and single-event effects on a color CMOS camera for space exploration," *IEEE Trans. Nucl. Sci.*, vol. 66, no. 1, pp. 104–110, Jan. 2019.

[17] P. W. Marshall, C. J. Dale, E. A. Burke, G. P. Summers, and G. E. Bender, "Displacement damage extremes in silicon depletion regions," *IEEE Trans. Nucl. Sci.*, vol. 36, no. 6, pp. 1831–1839, Dec. 1989.

[18] J. Bogaerts, B. Dierickx, G. Meynants, and D. Uwaerts, "Total dose and displacement damage effects in a radiation-hardened CMOS APS," *IEEE Trans. Electron Devices*, vol. 50, no. 1, pp. 84–90, Jan. 2003.

[19] J. W. Corbett and G. D. Watkins, "Production of divacancies and vacancies by electron irradiation of silicon," *Phys. Rev.*, vol. 138, no. 2A, pp. A555–A560, Apr. 1965.

[20] E. M. Donegani *et al.*, "Study of point- and cluster-defects in radiation-damaged silicon," *Nucl. Instrum. Methods Phys. Res. A, Accel. Spectrom. Detect. Assoc. Equip.*, vol. 898, pp. 15–23, Aug. 2018.

[21] J.-M. Belloir *et al.*, "Pixel pitch and particle energy influence on the dark current distribution of neutron irradiated CMOS image sensors," *Opt. Express*, vol. 24, no. 4, pp. 4299–4315, Feb. 2016.

[22] P. A. Martin, B. G. Streetman, and K. Hess, "Electric field enhanced emission from non-Coulombic traps in semiconductors," *J. Appl. Phys.*, vol. 52, no. 12, pp. 7409–7415, 1981.

[23] J. R. Srour and R. A. Hartmann, "Enhanced displacement damage effectiveness in irradiated silicon devices," *IEEE Trans. Nucl. Sci.*, vol. 36, no. 6, pp. 1825–1830, Dec. 1989.

[24] J. Bogaerts, B. Dierickx, and R. Mertens, "Enhanced dark current generation in proton-irradiated CMOS active pixel sensors," *IEEE Trans. Nucl. Sci.*, vol. 49, no. 3, pp. 1513–1521, Jun. 2002.

[25] J. R. Srour and D. H. Lo, "Universal damage factor for radiation-induced dark current in silicon devices," *IEEE Trans. Nucl. Sci.*, vol. 47, no. 6, pp. 2451–2459, Dec. 2000.

[26] S. Dhombres *et al.*, "Study of a thermal annealing approach for very high total dose environments," *IEEE Trans. Nucl. Sci.*, vol. 61, no. 6, pp. 2923–2929, Dec. 2014.

[27] J.-M. Belloir *et al.*, "Dark current spectroscopy on alpha irradiated pinned photodiode CMOS image sensors," *IEEE Trans. Nucl. Sci.*, vol. 63, no. 4, pp. 2183–2192, Aug. 2016.

[28] J. M. Belloir *et al.*, "Dark current spectroscopy in neutron, proton and ion irradiated CMOS image sensors: From point defects to clusters," *IEEE Trans. Nucl. Sci.*, vol. 64, no. 1, pp. 27–37, Jan. 2017.

[29] A. Le Roch *et al.*, "Radiation-induced defects in 8T-CMOS global shutter image sensor for space applications," *IEEE Trans. Nucl. Sci.*, vol. 65, no. 8, pp. 1645–1653, Aug. 2018.

[30] V. P. Markevich, A. R. Peaker, S. B. Lastovskii, L. I. Murin, and J. L. Lindström, "Defect reactions associated with divacancy elimination in silicon," *J. Phys., Condensed Matter*, vol. 15, no. 39, pp. S2779–S2789, Sep. 2003.

[31] J. Coutinho, R. Jones, S. Öberg, and P. R. Briddon, "The formation, dissociation and electrical activity of divacancy-oxygen complexes in Si," *Phys. B, Condensed Matter*, vols. 340–342, pp. 523–527, Dec. 2003.

[32] C. Virmontois *et al.*, "Dark current random telegraph signals in solid-state image sensors," *IEEE Trans. Nucl. Sci.*, vol. 60, no. 6, pp. 4323–4331, Dec. 2013.

[33] V. Goiffon, "Radiation effects on CMOS active pixel image sensors," in *Ionizing Radiation Effects in Electronics: From Memories to Imagers*. Boca Raton, FL, USA: CRC, 2015, pp. 295–332.

[34] C. Virmontois *et al.*, "Total ionizing dose versus displacement damage dose induced dark current random telegraph signals in CMOS image sensors," *IEEE Trans. Nucl. Sci.*, vol. 58, no. 6, pp. 3085–3094, Dec. 2011.

[35] A. P. Karmarkar, B. K. Choi, R. D. Schrimpf, and D. M. Fleetwood, "Aging and baking effects on the radiation hardness of MOS capacitors," *IEEE Trans. Nucl. Sci.*, vol. 48, no. 6, pp. 2158–2163, Dec. 2001.

[36] C. Inguimbert, P. Arnolda, T. Nuns, and G. Rolland, "'Effective NIEL' in silicon: Calculation using molecular dynamics simulation results," *IEEE Trans. Nucl. Sci.*, vol. 57, no. 4, pp. 1915–1923, Aug. 2010.